Chemical tuning of magnetic anisotropy and correlations in Ni$_{1-x}$Fe$_x$PS$_3$

Seungyeol Lee [1], Jaena Park,[1] Youngsu Choi,[1] Kalaivanan Raju,[2] Wei-Tin Chen [3,4]

Raman Sankar,[2,*] and Kwang-Yong Choi [5,†]

[1]*Department of Physics, Chung-Ang University, Seoul 06974, Republic of Korea*

[2]*Institute of Physics, Academia Sinica, Nankang, Taipei 11529, Taiwan, Republic of China*

[3]*Center for Condensed Matter Sciences and the Center of Atomic Initiative for New Materials, National Taiwan University, Taipei, Taiwan*

[4]*Taiwan Consortium of Emergent Crystalline Materials, Ministry of Science and Technology, Taipei, Taiwan*

[5]*Department of Physics, Sungkyunkwan University, Suwon, Republic of Korea*

We report the temperature and composition dependence of static magnetic susceptibility and Raman spectroscopic measurements on van der Waals antiferromagnets Ni$_{1-x}$Fe$_x$PS$_3$. The end members NiPS$_3$ and FePS$_3$ feature *XY*- and Ising-like magnetism, respectively, enabling chemical tuning of magnetic anisotropy and spin correlations. Ni$_{1-x}$Fe$_x$PS$_3$ shows a turnover from the *XY* to Ising anisotropy through $x \approx 0.1$. Although the *XY* anisotropy is rapidly suppressed on introducing Fe content, two-magnon scattering evidences the slow repression of short-range magnetic correlations deep inside the Fe-rich side. Counterintuitively, the two-magnon signal undergoes less renormalization of its energy with increasing x despite the larger spin number and enhanced classical magnetism. The disparate static and dynamic magnetic behaviors indicate the emergence of an exotic spin state in alloy van der Waals magnets.

I. INTRODUCTION

Dimensionality plays a key role in determining the magnetic and electric properties of materials. In this vein, magnetic van der Waals (vdW) materials stand out because magnetic planes are separated by a vdW gap. This gap effectively hinders superexchange paths between the layers, making them an ideal two-dimensional (2D) system. As such, vdW magnets offer a conspicuous platform to obtain a fundamental understanding of low-dimensional magnetism and to implement ultrathin spintronic device [1–6]. An overwhelming issue in this field is to tailor their physical properties by chemical, electrical, mechanical, and optical engineering towards achieving future applications.

Among magnetic vdW materials, MPX$_3$ (M = transition metal and X = S,Se) constitutes a versatile class in that these isostructural compounds accommodate three representative spin models: Ising, *XY*, and Heisenberg Hamiltonian [7–14]. MPX$_3$ (monoclinic space group $C2/m$) forms a layered honeycomb lattice of the metal M ions [8,15]. From a viewpoint of magnetism, FePS$_3$ realizes a $S = 2$ Ising antiferromagnet with $T_N = 123$ K [16,17], MnPS$_3$ is a $S = 5/2$ Heisenberg antiferromagnet with $T_N = 78$ K [18], and NiPS$_3$ is a $S = 1$ *XXZ*-type antiferromagnet below $T_N = 158$ K [13,19,20]. FePS$_3$ and NiPS$_3$ share zigzag-type magnetic structures, while MnPS$_3$ has a Néel-type magnetic ordering [21,22]. The Néel-type magnetic structure of MnPS$_3$ induces time and spatial symmetry breaking, bringing about a linear magnetoelectric effect that persists down to the ultrathin limit [23]. On the other hand, the persistence of Ising-like magnetic order down to monolayer FePS$_3$ enables an in-depth understanding of the Onsager and the Mermin-Wigner theorem [14,24,25]. This is in sharp contrast to the suppression of long-range magnetic order in the monolayer NiPS$_3$ that is tied to the Berezinskii-Kosterlitz-Thouless (BKT) transition predicted for a 2D *XY* spin system [12,26,27]. The isostructural family MPS$_3$, harboring the aforementioned three spin models, raises exciting prospects to explore exotic magnetic states through substitution of the cation M compositions.

Along this motivation, a distinct series of alloys (Ni, Fe, Mn)PS$_3$ have been investigated [28–33]. It was reported that spin-flop transition is extremely sensitive to an alloy composition in Ni$_{1-x}$Mn$_x$PS$_3$. The strong x dependence is ascribed to single-ion anisotropy involving trigonal distortions. The magnetic phase diagram for Mn$_{1-x}$Fe$_x$PS$_3$ encompasses a spin-glass and reentrant spin-glass state around $0.3 \leqslant x \leqslant 0.7$. The competition between the Néel- and zigzag-type ordering may be responsible for the spin-glass transition. Unlike Mn$_{1-x}$Fe$_x$PS$_3$, a series of Ni$_{1-x}$Fe$_x$PS$_3$ exhibits a smooth evolution of the magnetic ordering temperature. The salient feature is that the Ising anisotropy changes abruptly to the *XXZ*-type anisotropy at $x \approx 0.1$ [33]. As mentioned above, FePS$_3$ and NiPS$_3$ possess the identical zigzag magnetic ordering, defying the occurrence of magnetically disordered states. Thus Ni$_{1-x}$Fe$_x$PS$_3$ is a promising system to address unconventional spin dynamics associated with bond frustration. We stress that although its static magnetic properties are well investigated, little is known about dynamical fluctuations and spin correlations resulting from the competition between easy-plane and easy-axis anisotropies.

*Corresponding author: sankarndf@gmail.com

†Corresponding author: choisky99@skku.edu
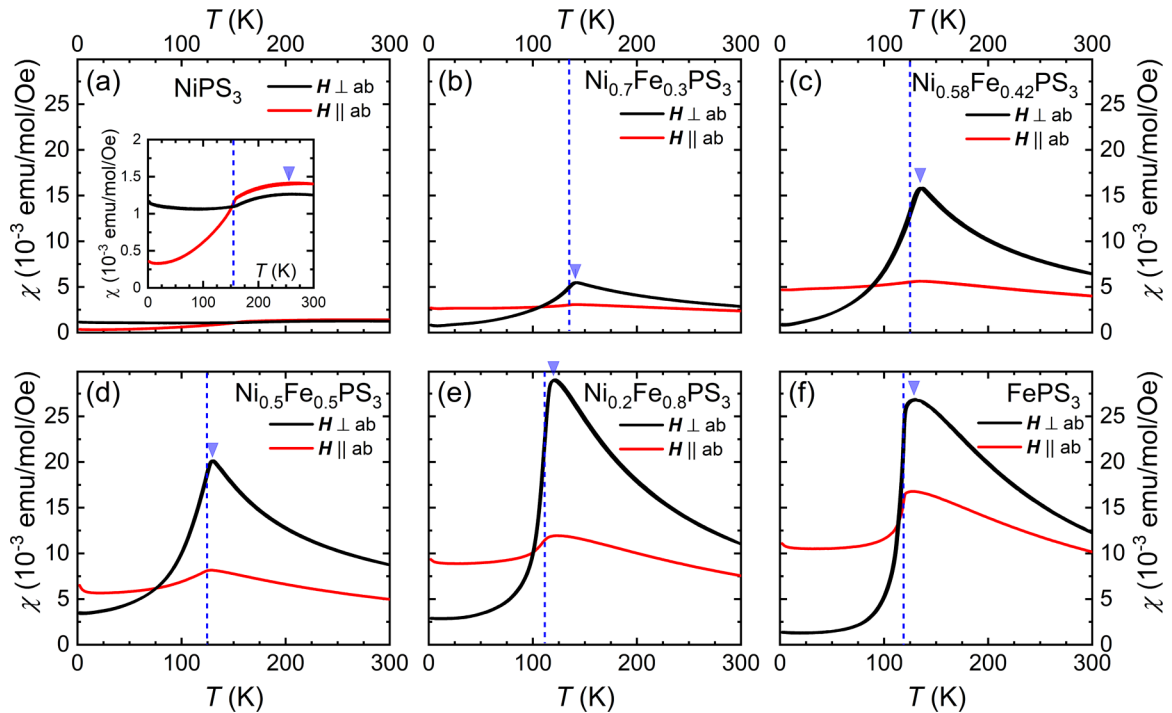
FIG. 1. Magnetic susceptibilities of $Ni_{1-x}Fe_xPS_3$ as a function of temperature measured at an external field of 1 T parallel (red) and perpendicular (black line) to the *ab* plane for (a) $x = 0$, (b) $x = 0.3$, (c) $x = 0.42$, (d) $x = 0.5$, (e) $x = 0.8$, and (f) $x = 1$. The vertical axes have the same scale for ease of comparison. The blue dashed lines mark the magnetic transition temperature T_N. The inverse triangles on top of the maximum of the magnetic susceptibilities denote the short-range ordering temperature T^*. The inset in (a) is a zoom of the magnetic susceptibility.

In the present work, we track magnetic correlations of $Ni_{1-x}Fe_xPS_3$ ($x = 0, 0.3, 0.5, 0.8$, and 1) as a function of temperature and composition. As a nondestructive spectroscopic technique, Raman spectroscopy is suitable for probing magnetic excitations through a double spin-flip process in antiferromagnets [34–36]. A thermal and composition dependence of two-magnon Raman scattering enables us to identify anomalous behaviors of short-range spin correlations that are incommensurate with *x*-dependent static magnetism.

II. EXPERIMENTAL DETAILS

The high-quality layered $Ni_{1-x}Fe_xPS_3$ single crystals were grown by a chemical vapor transport method using iodine as a transport agent. Initially, the polycrystalline powders were synthesized by the solid-state synthesis process under high vacuum conditions. The high-purity starting materials of iron (99.999%), nickel (99.999%), phosphorus (99.999%), and sulfur powder (99.999%) were weighted at a stoichiometric ratio and then sealed into the quartz tube with a diameter of 22 mm with 10^{-3} Torr pressure. The mixed compounds were heated and ground twice at 400 and 600 °C to make a single-phase compound. The 200 mg iodine was added into the polycrystalline samples and sealed by the tube dimension of $20 \times 22 \times 400$ mm^3 with 10^{-3} Torr. The tube was kept for growth at a two-zone furnace with the temperature range of 600–700 °C for 200 h. After completing the growth process, the furnace temperature was reduced to room temperature at a rate of 2°/min. The quartz tube was broken inside an argon-filled glovebox and collected good-quality single crystals.

The dc magnetization and magnetic susceptibility were measured as a function of temperature in an applied magnetic field of $\mu_0 H = 1$ T using a superconducting quantum interference device vibrating sample magnetometer (SQUID-VSM, Quantum Design). Raman scattering measurements were carried out in backscattering geometry with a micro-Raman spectrometer (XperRam200VN, NanoBase) equipped with an air-cooled charge-coupled device (Andor iVac Camera) and a holographic transmission diffraction grating (1800 grooves/mm). As an excitation source, we used a laser of the excitation line $\lambda = 532$ nm (DPSS SLM). The laser beam with $P = 100\ \mu$W was focused on a few-micrometer-diameter spot on the surface of the crystals using a ×40 magnification microscope objective. Rayleigh scattering was rejected to a lower cutoff frequency of 15 cm^{-1} using a notch filter. For temperature-dependent Raman experiments, the samples were mounted onto a liquid-He-cooled continuous flow cryostat by varying a temperature between 4.3 K and 400 K.

III. RESULTS AND DISCUSSION

A. Magnetic susceptibility and magnetization

Before proceeding, we mention that the static magnetic properties of $Ni_{1-x}Fe_xPS_3$ have been reported in early works [29,33]. Nonetheless, it will be advantageous to rediscuss the static magnetic susceptibility $\chi(T)$ and magnetization $M(H)$ for ease of the following comparison between static and dynamical magnetic behaviors.

In Fig. 1, we present the temperature and composition dependence of $\chi(T)$ of $Ni_{1-x}Fe_xPS_3$ ($x = 0, 0.3, 0.42, 0.5$,

0.8, and 1) measured at an external field of $\mu_0 H = 1$ T parallel (red) and perpendicular (black) to the ab plane. Our $\chi(T)$ data are in good agreement with the previously reported data [33]. With increasing x (Fe concentration), $\chi(T)$ is systematically enhanced up to $x = 0.8$ and then shows a slight decrease. In addition, the broad maximum [inverse triangle in the inset of Fig. 1(a)] observed in $x = 0$ turns into a sharp peak above $x = 0.3$, reflecting a switching of magnetic anisotropies between $x = 0$ and $x = 0.3$.

Next, we take a close look at the temperature dependence of $\chi(T)$. In the paramagnetic state of NiPS$_3$, $\chi(T)$ features the broad maximum at $T_{\max} \approx 220$ K ($\approx 1.6 T_N$), which is a hallmark of short-range spin correlations. The high-T $\chi(T)$ is larger for $\mu_0 H \parallel ab$ than $\mu_0 H \perp ab$, indicative of in-plane (or XXZ-like) magnetic anisotropy. As the spin-spin correlations are present over the whole measured temperature, we cannot make the Curie-Weiss analysis extract magnetic parameters. On approaching T_N, $\chi_{ab}(T)$ drops rapidly with the inflection point (vertical dashed line), while $\chi_c(T)$ is weakly T dependent. The $\chi_{ab}(T) \ll \chi_c(T)$ behavior in the magnetically ordered state confirms an easy-plane-type anisotropy. More than 30% of Fe substitution for Ni amplifies a classical magnetic behavior, inferred from the fact that the round maximum becomes sharp and the separation between $T_{\max}$ and T_N is drastically reduced. Besides, the $x \geqslant 0.3$ compositions bear the same Ising-type magnetism, namely, $\chi_c(T) > \chi_{ab}(T)$ in the high-T regime and $\chi_c(T) < \chi_{ab}(T)$ in the antiferromagnetically ordered state. On a qualitative level, the observed rapid repression of the low-dimensional magnetic correlations is ascribed to the combined effects of an increased spin number ($S = 1 \longrightarrow S = 2$), switching anisotropy ($XXZ \longrightarrow$ Ising), and chemical pressure. In particular, the chemical pressure increases interlayer interactions and modifies a degree of the trigonal distortion of (Fe/Ni)S$_6$ octahedra and spin-orbit coupling responsible for zero-field splitting. Remarkably, a previous study of Ni$_{1-x}$Fe$_x$PS$_3$ unveils that the anisotropy switching takes place even at a lower concentration $x = 0.1$ [33].

To identify magnetic transitions, we take a first derivative of $\chi(T)$ with respect to temperature. As evident in Figs. 2(a) and 2(b), $d\chi/dT$ shows a sharp peak at T_N. We plot the extracted T_N vs x in Fig. 2(c). With increasing x, T_N undergoes a systematic decrease from 162 K at $x = 0$ to 110 K at $x = 0.8$ and then shows an upturn to 119 K at $x = 1$. The essentially same x evolution of T_N has been reported in the literature [29,33], forming the minimum T_N around $x \approx 0.7$. As such, deviation from linear extrapolation in T_N between the two end materials should not be ascribed to sample inhomogeneities. Rather, this intrinsic behavior alludes to the existence of another ingredient, which fine-tunes magnetic interactions and anisotropies. As possible origins, we mention the chemical-pressure-induced trigonal distortions and the generation of Ni-Fe pairs whose magnetic behavior differs from Ni-Ni and Fe-Fe pairs. Shown in Fig. 2(d) is the temperature and composition dependence of the magnetic anisotropy defined as $\chi_\perp/\chi_\parallel$. For $x = 0$, $\chi_\perp/\chi_\parallel < 1$ in the high-T regime confirms the XY-like character of the Ni^{2+} magnetic moments. In combination with Ref. [33], our data showcase that the magnetic anisotropy changes from an XY-like to Ising-like anisotropy ($\chi_\perp/\chi_\parallel > 1$) above T_N at $x \geqslant 0.1$. The temperature evolution

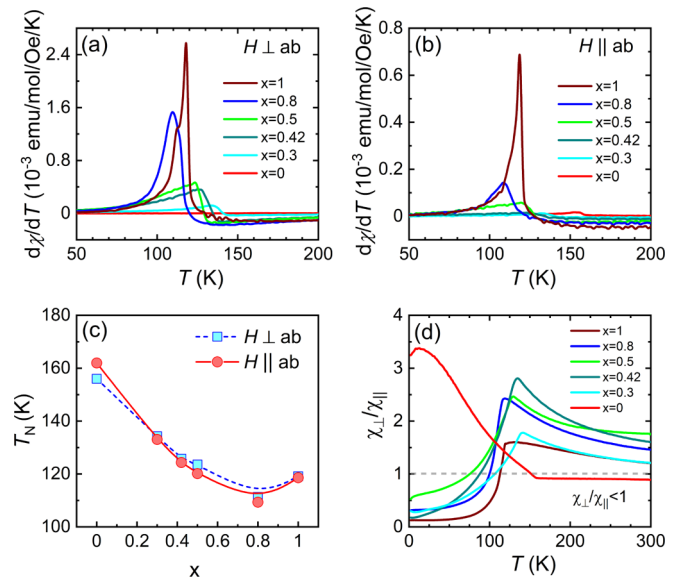

FIG. 2. First derivative of the magnetic susceptibility ($d\chi/dT$) with respect to temperature for (a) $\mu_0 H \perp ab$ and (b) $\mu_0 H \parallel ab$. (c) Néel temperature (T_N) vs Fe concentration (x) determined by a peak of $d\chi/dT$. (d) Temperature and composition dependence of the magnetic anisotropy defined as a ratio of $\chi_\perp$ to $\chi_\parallel$.

of the local spin anisotropy becomes the most pronounced around $x \approx 0.42$.

Figure 3 presents the $M(H)$ curves of Ni$_{1-x}$Fe$_x$PS$_3$ measured at $T = 2$ K for $\mu_0 H \perp ab$ and $\mu_0 H \parallel ab$. Overall, the low-field $M(H)$s display a linear field dependence as expected for antiferromagnets. With increasing Fe substitution, the
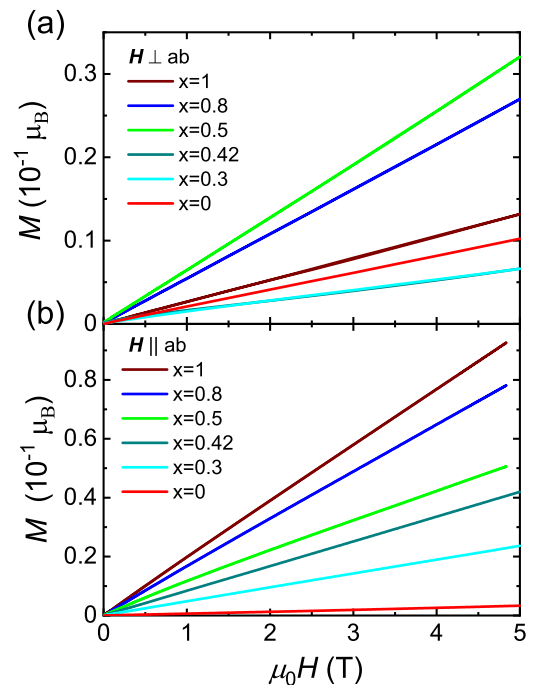

FIG. 3. Field-dependent magnetization of Ni$_{1-x}$Fe$_x$PS$_3$ ($x = 0$, 0.3, 0.42, 0.5, 0.8, and 1) for (a) $\mu_0 H \perp ab$ and (b) $\mu_0 H \parallel ab$. The temperature was fixed to $T = 2$ K.
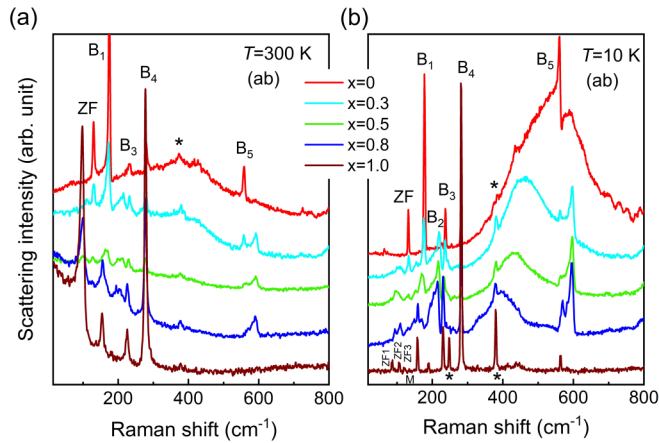
FIG. 4. Raman spectra of $Ni_{1-x}Fe_xPS_3$ ($x = 0$, 0.3, 0.5, 0.8, and 1) at (a) $T = 300$ K and (b) $T = 10$ K measured in cross (*ab*) polarization. B_i ($i = 1$–5) labels symmetry-allowed B_g phonon modes. The asterisks denote forbidden A_g modes, which become intense in the magnetically ordered state of Fe-rich samples. Three ZF_i ($i = 1$–3) represent zone-folded phonons and M stands for one-magnon excitation.
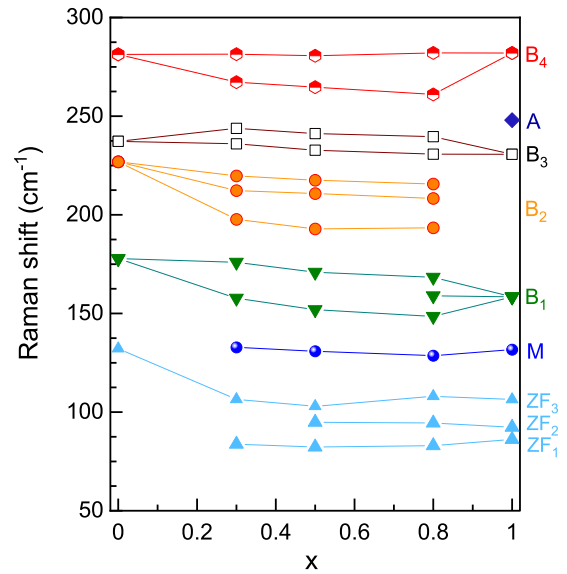

FIG. 5. Fe-substitution dependence of the phonon frequencies at 10 K. For the mixed samples, the B_g phonons exhibit two- or three-mode behavior.

in-plane $M_\parallel(H)$ is systematically enhanced in the measured low-field range, being consistent with the increment of Ising-type anisotropy with x. On the other hand, the out-of-plane $M_\perp(H)$ features an intriguing x dependence. The low-field $M_\perp(H)$ first increases up to $x = 0.5$ and then decreases towards $x = 1$. This trend coincides with the composition dependence of $\chi_\perp/\chi_\parallel$ plotted in Fig. 2(d). Thus we conclude that the Ising anisotropy is the largest around $x \approx 0.5$, alluding to a nontrivial role of chemical pressure in modulating the magnetic anisotropy.

B. Phonon excitations

In Fig. 4, we compare Raman spectra of $Ni_{1-x}Fe_xPS_3$ measured at $T = 300$ K and 10 K in (*ab*) polarization. We have chosen this cross-polarization scattering configuration to maximize information about magnetic excitations. We refer to the previous Raman works for the complete assignments and full descriptions of phonon modes in other polarizations [12–14,37–44]. We further comment that the end members $NiPS_3$ and $FePS_3$ have intensively investigated to understand fundamental magnetism in the 2D limit. Spectral changes induced by magnetic ordering are mainly monitored as a function of layer number and temperature. For the Ising-like vdW antiferromagnet $FePS_3$, a long-range magnetic order is retained down to a single layer [14,40,43]. In contrast, long-range magnetic ordering vanishes in the monolayer regime of mechanically exfoliated $NiPS_3$, being consistent with a BKT transition [13]. However, the thermal evolution of magnetic correlations is hardly addressed in relation to magnetic anisotropy, which is the focus of this study.

According to the factor group analysis, we expect a total of 15 irreducible representation of Raman-active phonon modes $\Gamma_{raman} = 8A_g(xx) + 7B_g(xy)$. We note that only the B_g modes are symmetry allowed in the cross polarization. Out of the anticipated $7B_g$ phonons, we could identify five B_g modes, labeled B_i ($i = 1$–5), for the stoichiometric compounds $NiPS_3$

and $FePS_3$. Two weak peaks marked by the asterisks are ascribed to the symmetry-forbidden A_g modes stemming from leakage of polarization, local strain, or stacking disorders. For $FePS_3$, with lowering temperature below T_N, the two A_g modes become pronounced and the zone-folded ZF mode is split into four peaks. The three ZF_i ($i = 1$–3) peaks are spin-order-induced phonon modes arising from the Brillouin-zone folding by a magnetic superstructure [13]. The M peak is assigned to one-magnon scattering [43]. In the intermediate mixed compounds, one or two phonon peaks are newly activated for each B_i mode (see Fig. 5). In addition to the phonon excitations, we observe a broad magnetic background, which shows a notable temperature and composition dependence. With increasing x, the magnetic Raman signal shows a red-shift and a reduction in its intensity (see the next section for details).

In Fig. 5, we detail the composition dependence of the phonon frequencies below 300 cm^{-1} measured at 10 K. The phonon modes B_i ($i = 2$–5) involve vibrations of the $(P_2S_6)^{4-}$ unit, which is located in the center of the (Ni/Fe) honeycomb lattice [40,43]. On the other hand, the low-frequency B_1 mode contains motion of the metal M^{2+} ion. As such, the low-frequency modes are largely affected by the metal cation Ni^{2+}/Fe^{2+} substitution. Indeed, with decreasing frequency and increasing x, the redshift becomes pronounced. The softening phonon frequency with increasing x is linked to the fact that the Ni^{2+} ion is heavier than the Fe^{2+} ion. Consistently, the lattice constants contract 1–2% preferentially in the *ab* plane with decreasing x [29,33].

In addition, the intermediate mixed compounds entail additional phonon modes. Specifically, the B_3 and B_4 phonons are split into two peaks and the B_1 and B_2 modes are split into three peaks. The two-mode behavior is naturally expected for alloys since the same normal modes of the two end members are distinct in their frequencies. However, the three-mode splitting raises the possibility that local bonding geometries,
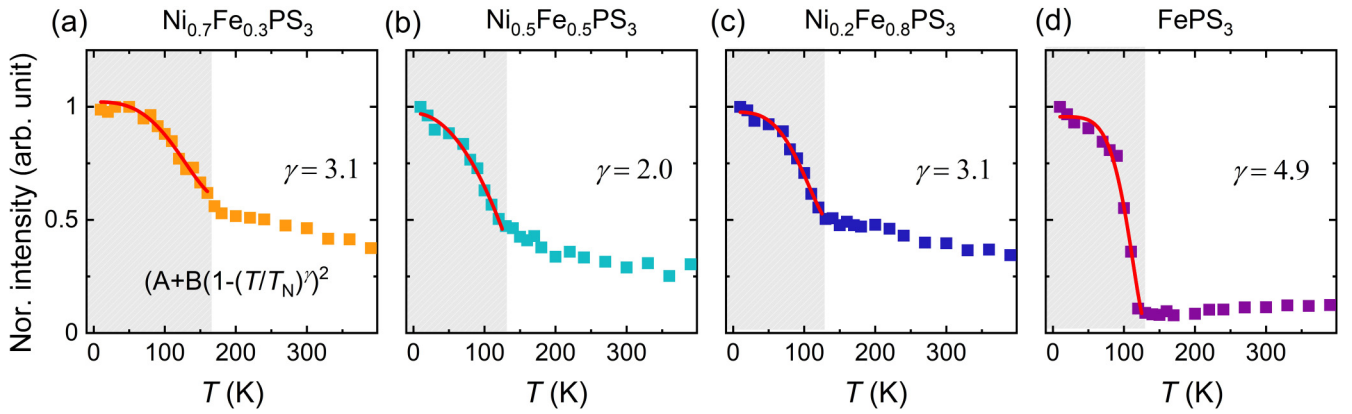
FIG. 6. Normalized intensity of the 380 cm^{-1} A_g mode as a function of temperature and composition. The shaded gray area denotes the temperature interval, in which spin-dependent Raman scattering is observed. The solid lines are fits to the expression $I_{\text{s-RS}}(T) \sim |A + B[1 - (\frac{T}{T_N})]^{\gamma}|^2$ as described in the text.

stacking disorders, and magnetic environments are slightly modified under chemical substitution. Thus Raman-inactive or symmetry-forbidden phonons may be activated and doubly degenerate modes may split [45]. We further note that the zone-folded phonons and one-magnon mode are discernible in the low-temperature spectrum for $x \geqslant 0.3$. The Raman spectrum of NiPS$_3$ shows no evidence of one-magnon scattering. The spin-dependent Raman scattering seems to be appreciable only for the Fe^{2+} containing compounds.

Next, we pay our attention to the 380 cm^{-1} A_g mode, which is originally symmetry forbidden, yet appears due to phonon-mode leakage. We can use the 380 cm^{-1} mode as a local probe of antiferromagnetic ordering [12,40,43]. The phonon parameters (phonon frequency and linewidth) cannot be reliably traced due to their weak intensity. In consideration of this situation, we restrict ourselves to the integrated intensity as plotted in Fig. 6. For all $x \geqslant 0.3$, the phonon intensity exhibits an abrupt increase with the onset of the Néel temperature (indicated by gray shadings). In spin-dependent Raman scattering [46], the increasing Raman intensity is given by the square of the spin correlation function, $I_{\text{s-RS}}(T) \sim |A + B[1 - (\frac{T}{T_N})]^{\gamma}|^2$, by assuming a phenomenological expression of the spin-spin correlation $\langle \mathbf{S}_i \cdot \mathbf{S}_{i+1} \rangle \sim [1 - (\frac{T}{T_N})]^{\gamma}$. The phenomenological parameter γ is scattered around the values of 2.0–4.9, bearing no concrete physical meaning. Here, A (gauging nonmagnetic contribution) and B are constants. For FePS$_3$, the nonmagnetic contribution is negligibly small with $A \sim 0.1$. With increasing Ni concentration, the spin-dependent scattering intensity weakens with $A \approx 0.5$–0.6. The diminishing spin-dependent contribution with decreasing x is partly ascribed to a decreasing spin number ($S = 2 \longrightarrow S = 1$). However, the lacking systematic trend may be due to local strains inevitably occurring in alloy compounds, which affect a phonon scattering intensity.

C. Two-magnon Raman scattering

We now turn to the Raman response of two-magnon (2M) excitations and will expound their temperature and composition evolution. In antiferromagnets, the 2M spectrum arising from double spin-flip processes conveys information about spin dynamics and the energy scale of exchange interactions [34,47].

As shown in Fig. 7(a), the $T = 10$ K magnetic spectrum of NiPS$_3$ exhibits a rather symmetric line shape positioned around $\omega_{2M} = 546$ cm^{-1}. With increasing temperature, the magnetic spectrum broadens and shifts to lower energies. For low-dimensional magnets, the 2M spectrum persists well above the ordering temperature as it mainly reflects the temperature dependence of short-wavelength magnon energies and lifetimes [48]. With increasing Fe content [Figs. 7(b)– 7(e)], ω_{2M} of the 2M scattering shifts to 394 cm^{-1} at $x = 0.8$. The well-resolved magnetic continuum at low temperatures vanishes for the pristine FePS$_3$. At room temperature, the coherent magnetic excitation progressively evolves to a quasielastic response with increasing x. In Figs. 7(f)–7(j), we present the color contour plots of the 2M scattering intensity in the $T - \omega$ plane after subtracting the phonon peaks from the raw spectra. The temperature and composition trend becomes evident. On heating toward T_N, the lower-cutoff energy ω_{lower} undergoes an order-parameter-like softening. We deduce the Néel temperature T_{N^*} by extrapolating ω_{lower} to 0 cm^{-1} (horizontal dotted line). We note that the low-energy spectral weight is dictated by long-wavelength magnons, while the peak intensity by short-range magnons. The latter enables us to introduce another characteristic temperature T^* (horizontal dotted line), at which the 2M maximum turns into a quasielastic response. We find that the larger the spin number (Fe content) is, the stronger are the changes of spectral weights at an energy scale of T_{N^*}.

To comprehend the thermal damping of the 2M spectra, we resort to the Fleury and Loudon theory of describing magnetic Raman scattering in Mott insulators [34]. In a nutshell, light can excite magnons in pairs through the virtual electron hopping process similar to exchange interactions. In this exchange-scattering mechanism, thus, the Raman operator is proportional to a spin Hamiltonian $\mathcal{R} \propto \sum_{i,j} \mathbf{S}_i \cdot \mathbf{S}_j$. The Fleury and Loudon mechanism provides a natural rationale for the vanishing 2M signal in FePS$_3$ since the Ising-like Hamiltonian $\mathcal{H} \propto \sum_{i,j} \mathbf{S}_i^z \cdot \mathbf{S}_j^z$ commutes with the Raman operator $\mathcal{R} \propto \sum_{i,j} \mathbf{S}_i^z \cdot \mathbf{S}_j^z$ with bond-dependent polarization term, that is, $[\mathcal{H}, \mathcal{R}] = 0$. In the classical treatment, the 2M peak energy
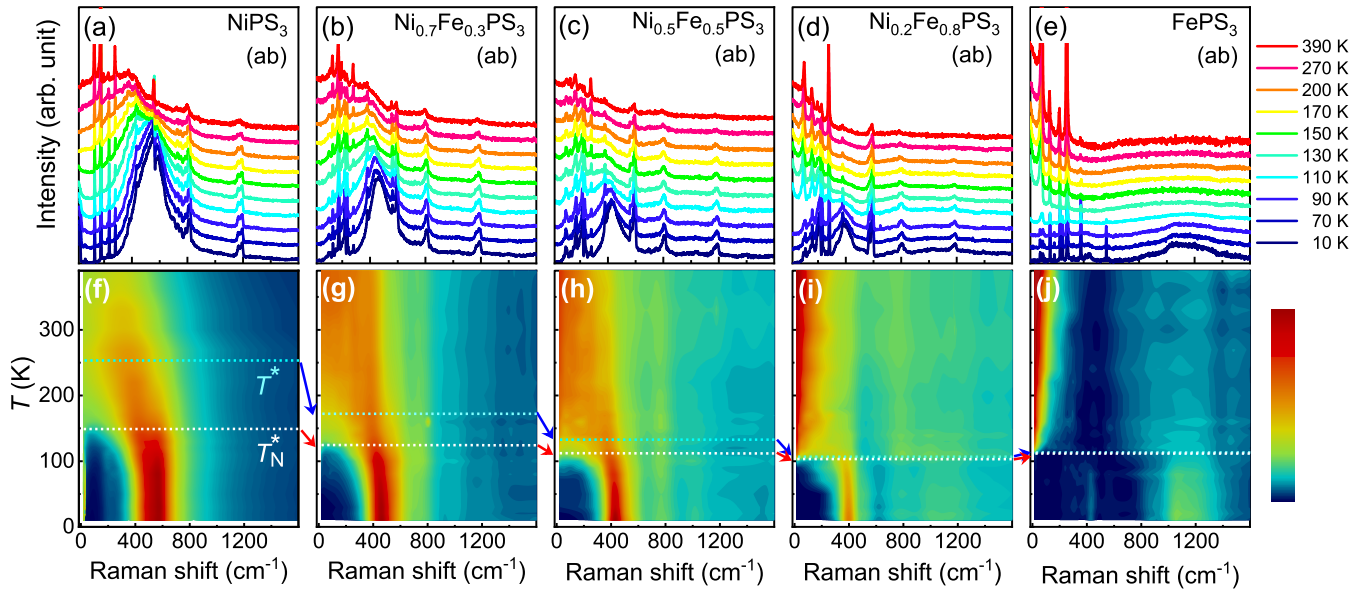
FIG. 7. Temperature- and composition-dependent Raman spectra of $Ni_{1-x}Fe_xPS_3$ for (a) $x = 0$, (b) $x = 0.3$, (c) $x = 0.5$, (d) $x = 0.8$, and (e) $x = 1$ measured in (*ab*) polarization. (f)–(j) Contour plot of the two-magnon scattering intensity in the temperature-Raman-shift plane after subtracting phonon peaks. The horizontal dotted lines denote the Néel temperature T_{N*} and short-range ordering temperatures T^*, which are identified from a thermal evolution of the low-energy cutoff and the peak energy.

ω_{2M} allows the estimation of the exchange coupling constant by the relation $\sum_i J_i(2z_iS - 1)$, where J_i is the exchange constant, z_i is the number of neighboring spins, and S is the spin quantum number. Given that a $J_1 - J_3$ spin Hamiltonian provides the minimal model of $NiPS_3$ ($S = 1$), the 2M peak position $\omega_{2M} = 546 \, cm^{-1}$ corresponds to $5(J_1 + J_3)$, yielding $J_1 + J_3 = 13.6$ meV. Here, the number of the nearest and third-nearest neighboring spins are $z_1 = z_3 = 3$. Noticeably, the obtained value is comparable to $J_1 = -3.8$ meV and $J_3 = 13.8$ meV [20], although the 2M peak alone is insufficient to determine each J_i. By assuming that $\omega_{2M} = 461 \, cm^{-1}$ is the average of 70% Ni-Ni pairs and 30% Fe-Fe pairs (neglecting Ni-Fe pairs), we obtain $J_1 + J_3 = 3.25$ meV for $FePS_3$. The reduction of J_i in $FePS_3$ accounts for the concomitant narrowing and softening of the 2M spectral weight with x. We further comment that, if the 2M scattering is allowed due to residual terms, its spectral weight would appear below $250 \, cm^{-1}$.

In Fig. 8(a), we plot the normalized 2M frequency of $Ni_{1-x}Fe_xPS_3$ ($x = 0$, 0.3, 0.5, and 0.8) vs reduced temperature T/T_N. For $NiPS_3$, the magnon-pair spectral weight is renormalized by $\sim$15% at T_N, typical for 2D $S = 1$ antiferromagnets [48]. With increasing Fe content (spin number), the peak-energy renormalization is reduced to 10%. A similar tendency is seen above T_N. This is at odds with the common wisdom that the renormalization and damping of the 2M spectral weight becomes stronger as the dimension and spin number increase. Unlike the thermal renormalization of the 2M parameters, the short-range magnetic correlations (called paramagnons) persist to higher temperatures with increasing Ni substitution. This seemingly inconsistent observation implies that the alloy compounds cannot be described by the simple mixture of $S = 1$ XXZ and $S = 2$ Ising spin Hamiltonians. In the intermediate compositions, Ni-Fe bond pairs are present in addition to Ni-Ni and Fe-Fe pairs, which may
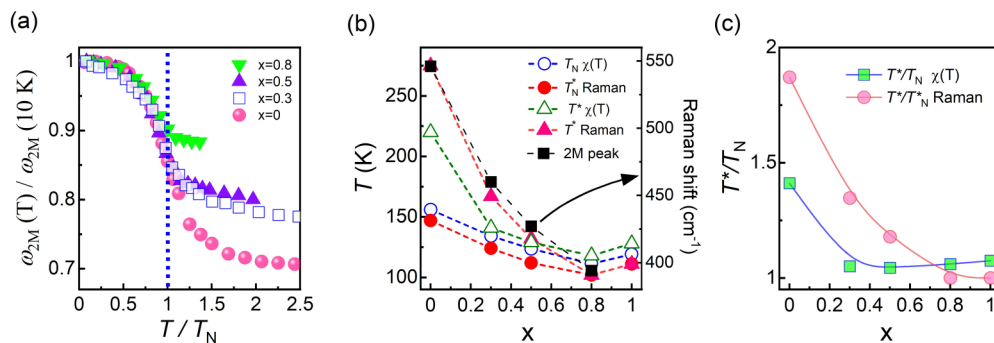

FIG. 8. (a) Normalized two-magnon energy vs normalized temperature for $x = 0$, 0.3, 0.5, and 0.8. The vertical dashed line marks the Néel temperature. (b) x dependence of the Néel temperature and short-range ordering temperatures T_N and T^* determined by the static magnetic susceptibility $\chi(T)$ and T_{N*} and T^* by the two-magnon scattering. The two-magnon peak energy (black squares) is correlated with the thermal damping temperature of the two-magnon peak (red circles). (c) Ratio T^*/T_N extracted from the $\chi(T)$ and Raman data as a function of x.

introduce bond frustration. At present, nothing is known about the character of Ni-Fe exchange interactions, which may lead to an exotic magnetic state, deserving future investigations.

In Fig. 8(b), we summarize the Néel and short-range ordering temperatures extracted from the $\chi(T)$ and 2M Raman data. It is evident that T_N deduced from $\chi(T)$ goes hand in hand with the 2M Raman-determined transition temperature T_{N^*}. The small underestimate of T_{N^*} by the Raman spectra is due to the uncertainty of tracking the complete thermal destabilization of long-wavelength magnons in the vicinity of T_N. We note that ω_{2M} (black squares) is inextricably correlated with the thermal damping of short-wavelength magnons. In stark contrast, the short-range ordering temperature T^* reveals a disparity between the static and dynamic probes. To showcase this trend, we plot the ratio T^*/T_N vs x in Fig. 8(c). We observe that T^*/T_N based on the $\chi(T)$ data shows the quick suppression through $x = 0.3$, while T_{N^*} derived from the Raman data exhibits a rather gradual decrease to $x = 0.8$. This suggests that the short-range spin correlations are slowly diminished with increasing high-spin Fe^{2+} content, although the static magnetism is quickly switched to an Ising-like behavior.

IV. CONCLUSION

We have conducted a systematic magnetic susceptibility and Raman spectroscopic study of quasi-2D vdW materials $Ni_{1-x}Fe_xPS_3$. These alloy compounds enable chemical tuning of easy-plane and easy-axis anisotropies by Fe-for-Ni substitution.

The static magnetic data reveal that an XY-like anisotropy is switched to an Ising-like one upon introduction of Fe con-

centration as small as 10%, if combined with Selter's data [33]. The sharp maximum of $\chi(T)$ and the small separation between the long-range ordering temperature T_N and the short-range ordering temperature T^* advocate that classical magnetism dictates Fe-rich samples. Unexpectedly, dynamic magnetism based on two-magnon Raman scattering shows a distinct x evolution. Short-range magnetic correlations near the Brillouin zone boundary are rather gradually suppressed against the Fe-for-Ni substitution. More strikingly, the thermal renormalization of the two-magnon energy is obviously reduced with x despite the quick repression of XY-like quantum fluctuations. Taken together, a small amount of chemical substitution stabilizes quickly the Ising-like magnetism against the XY-like magnetism. On the other hand, the dynamic magnetism pertaining to short-range correlated spins is not quickly quenched in the presence of competing Ising- and XY-like interactions despite the classical magnetism that prevails. We call for future investigations on understanding the origins of disparate static and dynamic magnetic behaviors and the possible emergence of an exotic spin state in alloy vdW magnets.

[1] M. A. McGuire, Crystals **7**, 121 (2017).

[2] K. S. Burch, D. Mandrus, and J.-G. Park, Nature (London) **563**, 47 (2018).

[3] C. Gong and X. Zhang, Science **363**, eaav4450 (2019).

[4] W. Zhang, P. K. J. Wong, R. Zhu, and A. T. S. Wee, InfoMat. **1**, 479 (2019).

[5] M. Gibertini, M. Koperski, A. F. Morpurgo, and K. S. Novoselov, Nat. Nanotechnol. **14**, 408 (2019).

[6] S. Yang, T. Zhang, and C. Jiang, Adv. Sci. **8**, 2002488 (2021).

[7] G. Leflem, R. Brec, G. Ouvard, A. Louisy, and P. Segransan, J. Phys. Chem. Solids **43**, 455 (1982).

[8] R. Brec, Solid State Ion. **22**, 3 (1986).

[9] N. Kurita and K. Nakao, J. Phys. Soc. Jpn. **58**, 610 (1989).

[10] N. Chandrasekharan and S. Vasudevan, J. Phys.: Condens. Matter **6**, 4569 (1994).

[11] V. Zhukov, S. Alvarez, and D. Novikov, J. Phys. Chem. Solids **57**, 647 (1996).

[12] J. U. Lee, S. Lee, J. H. Ryoo, S. Kang, T. Y. Kim, P. Kim, C. H. Park, J. G. Park, and H. Cheong, Nano. Lett. **16**, 7433 (2016).

[13] K. Kim, S. Y. Lim, J.-U. Lee, S. Lee, T. Y. Kim, K. Park, G. S. Jeon, C.-H. Park, J.-G. Park, and H. Cheong, Nat. Commun. **10**, 345 (2019).

[14] K. Kim, K. Park, S. Son, C.-H. Park, S. Y. Lim, J. Kim, J.-U. Lee, S. Lee, J.-G. P. Pilkwang, and H. Cheong, 2D Mater. **6**, 041001 (2019).

[15] G. Ouvrard, R. Brec, and J. Rouxel, Mater. Res. Bull. **20**, 1181 (1985).

[16] P. A. Joy and S. Vasudevan, Phys. Rev. B **46**, 5425 (1992).

[17] D. Lancon, H. C. Walker, E. Ressouche, B. Ouladdiaf, K. C. Rule, G. J. McIntyre, T. J. Hicks, H. M. Rønnow, and A. R. Wildes, Phys. Rev. B **94**, 214407 (2016).

[18] A. R. Wildes, B. Roessli, B. Lebech, and K. W. Godfrey, J. Phys.: Condens. Matter **10**, 6417 (1998).

[19] A. R. Wildes *et al.*, Phys. Rev. B **92**, 224408 (2015).

[20] D. Lancon, R. A. Ewings, T. Guidi, F. Formisano, and A. R. Wildes, Phys. Rev. B **98**, 134414 (2018).

[21] M. J. Coak, D. M. Jarvis, H. Hamidov, C. R. S. Haines, P. L. Alireza, C. Liu, S. Son, I. Hwang, G. I. Lampronti, D. Daisenberger, P. Nahai-Williamson, A. R. Wildes, S. S. Saxena, and J. G. Park, J. Phys.: Condens. Matter **32**, 124003 (2020).

[22] N. Sivadas, M. W. Daniels, R. H. Swendsen, S. Okamoto, and D. Xiao, Phys. Rev. B **91**, 235425 (2015).

[23] H. Chu, C. J. Roh, J. O. Island, C. Li, S. Lee, J. Chen, J.-G. Park, A. F. Young, J. S. Lee, and D. Hsieh, Phys. Rev. Lett. **124**, 027601 (2020).

[24] L. Onsager, Phys. Rev. **65**, 117 (1944).

[25] N. D. Mermin and H. Wagner, Phys. Rev. Lett. **17**, 1307 (1966).

[26] V. L. Berezinskii, Zh. Eksp. Teor. Fiz. **59**, 907 (1970).

[27] J. M. Kosterlitz and D. J. Thouless, J. Phys. C: Solid State Phys. **6**, 1181 (1973).

[28] T. Masubuchi, H. Hoya, T. Watanabe, Y. Takahashi, S. Ban, N. Ohkubo, K. Takase, and Y. Takano, J. Alloy Compd. **460**, 668 (2008).

[29] R. R. Rao and A. K. Raychaudhuri, J. Phys. Chem. Solid **53**, 577 (1992).

[30] A. Bhutani, J. L. Zuo, R. D. McAuliffe, C. R. de la Cruz, and D. P. Shoemaker, Phys. Rev. Mater. **4**, 034411 (2020).

[31] J. N. Graham, M. J. Coak, S. Son, E. Suard, J.-G. Park, L. Clark, and A. R. Wildes, Phys. Rev. Mater. **4**, 084401 (2020).

[32] Y. Shemerliuk, Y. Zhou, Z. Yang, G. Cao, A. U. B. Wolter, B. Büchner, and S. Aswartham, Electron. Mater. **2**, 284 (2021).

[33] S. Selter, Y. Shemerliuk, M.-I. Sturza, A. U. B. Wolter, B. Büchner, and S. Aswartham, Phys. Rev. Mater. **5**, 073401 (2021).

[34] P. A. Fleury and R. Loudon, Phys. Rev. **166**, 514 (1968).

[35] K. Kim, J.-U. Lee, and H. Cheong, Nanotechnology **30**, 452001 (2019).

[36] D. Wulferding, Y. S. Choi, W. J. Lee, and K.-Y. Choi, J. Phys.: Condens. Matter **32**, 043001 (2020).

[37] M. Balkanski, M. Jouanne, G. Ouvrard, and M. Scagliotti, J. Phys. C: Solid State Phys. **20**, 4397 (1987).

[38] M. Bernasconi, G. L. Marra, G. Benedek, L. Miglio, M. Jouanne, C. Julien, M. Scagliotti, and M. Balkanski, Phys. Rev. B **38**, 12089 (1988).

[39] T. Sekine, M. Jouanne, C. Julien, and M. Balkanski, Phys. Rev. B **42**, 8382 (1990).

[40] X. Wang, K. Du, Y. Y. Fredrik Liu, P. Hu, J. Zhang, Q. Zhang, M. H. S. Owen, X. Lu, C. K. Gan, P. Sengupta, C. Kloc, and Q. Xiong, 2D Mater. **3**, 031009 (2016).

[41] Y.-J. Sun, Q.-H. Tan, X.-L. Liu, Y.-F. Gao, and J. Zhang, J. Phys. Chem. Lett. **10**, 3087 (2019).

[42] A. V. Peschanskii, T. Ya. Babuka, K. E. Glukhov, M. Makowska-Janusik, S. L. Gnatchenko, and Yu. M. Vysochanskii, Low Temp. Phys. **45**, 1082 (2019).

[43] A. McCreary, J. R. Simpson, T. T. Mai, R. D. McMichael, J. E. Douglas, N. Butch, C. Dennis, R. Valdes Aguilar, and A. R. Hight Walker, Phys. Rev. B **101**, 064416 (2020).

[44] A. Ghosh, M. Palit, S. Maity, V. Dwij, S. Rana, and S. Datta, Phys. Rev. B **103**, 064431 (2021).

[45] E. Anastassakis and E. Burstein, J. Phys. C: Solid State Phys. **5**, 2468 (1972).

[46] N. Suzuki and H. Kamimura, J. Phys. Soc. Jpn. **35**, 985 (1973).

[47] S. Rosenblum, A. H. Francis, and R. Merlin, Phys. Rev. B **49**, 4352 (1994).

[48] M. G. Cottam and D. J. Lockwood, *Light Scattering in Magnetic Solids* (Wiley, New York, 1986).